

## **PREDICTION OF CRUD DEPOSITION IN A CANDU-SCWR CORE THROUGH CORROSION PRODUCT SOLUBILITY AND TRANSPORT MODELLING**

**W.G. Cook and R.P. Olive**

University of New Brunswick, New Brunswick, Canada

### **Abstract**

Corrosion-product deposition in-core is particularly troublesome for a nuclear reactor because of potentially reduced heat transfer leading to fuel failure and the possibility of activation of the deposits leading to activity transport through the entire system. In this work, the magnitude and location of crud deposits in and around the core of a simplified CANDU-SCWR design are estimated through a corrosion-product solubility and transport model. The model predicts deposition loading to decrease as the coolant goes from saturated in corrosion products to undersaturated. Additionally, it was observed that increasing operational pressure increases core deposits while shifting the location of the initiation of deposition to further up the fuel channel.

### **1. Introduction**

As the second decade of the 21<sup>st</sup> century begins, the focus of organisations continues to move toward so-called “green” products and technologies. Many companies have had to change their existing ways of doing business in order to operate in a more environmentally friendly manner. The power industry is no exception. Power production that results in high levels of greenhouse gas emissions are gradually being phased out in favour of their more “clean” counterparts. This shift has the potential to be favourable to the nuclear power industry as nuclear plants operate with relatively low levels of carbon dioxide emissions. Additionally, nuclear fuel has a high energy density meaning that a large amount of energy can be produced from a small amount of fuel, leading to less waste. These characteristics make nuclear power an attractive generation option as this century continues to unfold. However, even with these advantages, the production of electricity from nuclear reactors can improve even further by moving toward the so-called Generation IV reactors. The premise of these new reactors is that their design will be more proliferation resistant, more economical to build, inherently safe, and more efficient in the transfer of energy than the reactors currently employed.

One of the more promising Generation IV reactors is the Supercritical Water-cooled Reactor (SCWR). The SCWR employs supercritical water as its coolant and can realize efficiencies of ~50% because of the high temperature of coolant exiting the reactor (up to 625°C in some designs) [1]. This is a marked improvement over the efficiencies (~33%) of the currently operated nuclear reactors: the Pressurized Water Reactor (PWR), the Boiling Water Reactor (BWR), and the Canadian Deuterium Uranium Reactor (CANDU). The currently envisaged SCWR design is a direct cycle with no steam generator which will reduce the capital cost of plant construction. The lack of a steam generator means the SCWR will be similar to a BWR but without a phase separation in the core since the coolant will be above the critical temperature of water. Material selection and chemistry control will be extremely challenging because of the high operating pressure (~25 MPa) and the significant change in physical properties as water traverses its critical point.

The potential for corrosion-product deposition in the SCWR core is a problem that must be evaluated during reactor design, including the selection of materials and water chemistry. Burrill

predicted the magnitude of corrosion product deposition for a CANDU-6 type fuel channel in which the coolant enters at 350°C and exits at 384°C. He found that the magnitude of deposition was strongly dependent on the saturation level of the coolant in dissolved iron (with saturated coolant resulting in the largest amount of in-core deposits) [2]. Corrosion products depositing on the fuel bundles can result in reduced heat transfer to the coolant and eventually to fuel overheating and failure. Additionally, core deposits have the potential to become neutron activated and, upon transport to the turbine or other downstream components, result in the potential for significant worker dose. In order to find ways to minimize these effects, a good understanding of the solubility and transport of corrosion products under supercritical conditions is essential. Solubility influences the corrosion of materials, the dissolution and deposition of corrosion products and is dependent upon temperature, pressure, pH, and redox conditions [3].

## 2. Supercritical Water Properties

As the temperature of water approaches and traverses the thermodynamic critical point, its physical properties undergo dramatic changes. Figure 1 (a) shows the effect of increasing temperature on the heat capacity of water with pressure. Figure 1 (b) and (c) show the effect of increasing temperature on the density and dielectric constant of water, respectively. Figure 1 (d) illustrates the effect of increasing temperature on the pH of neutral water.

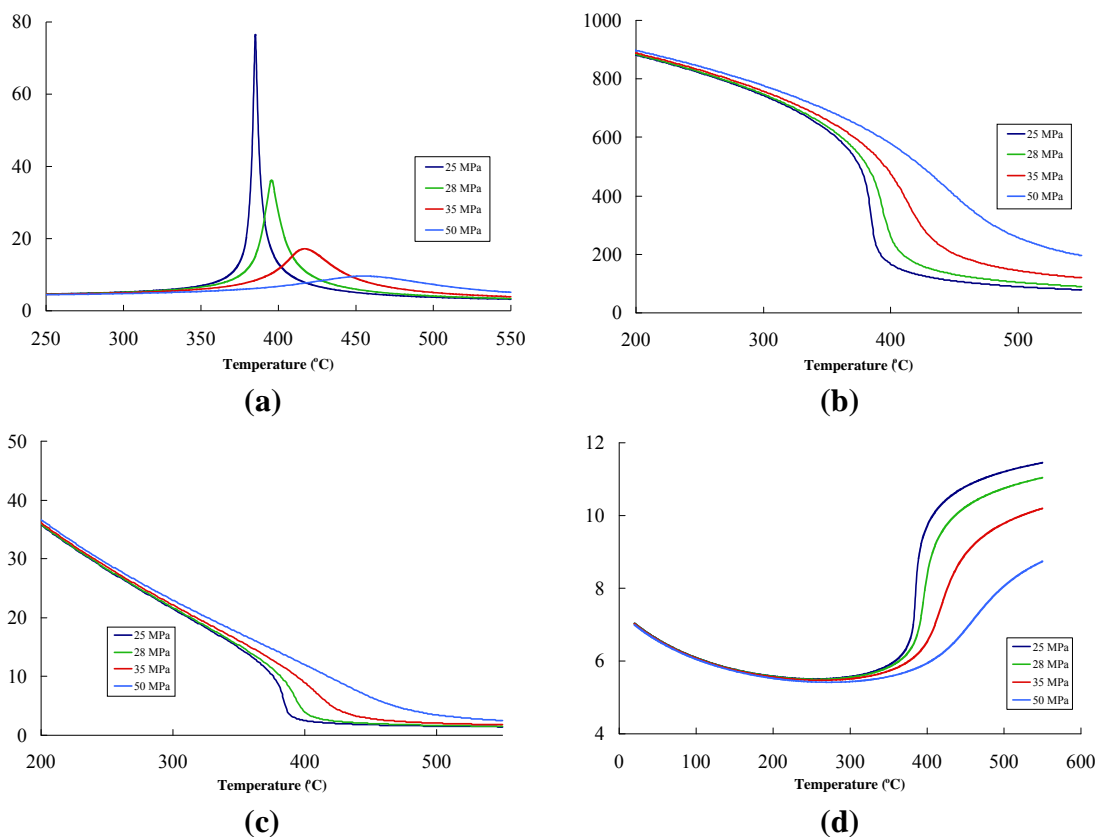


**Figure 1. (a) Heat capacity, (b) density, (c) dielectric constant and (d) pH of neutral water as a function of temperature and pressure.**

For a given pressure, the heat capacity passes through a maximum as illustrated in Figure 1(a). It should be noted that the maximum decreases and shifts to a higher temperature as the pressure is

increased following the “pseudo-critical” point. Figure 1(b) shows that the density of water drops dramatically at the pseudo-critical point. As temperature increases, the extent of hydrogen bonding decreases which hence lowers the density. With increasing pressure, the decrease in density becomes a more smooth transition as opposed to the sharp drop experienced at the pseudo-critical point for lower pressures.

A key parameter for the behaviour of dissolved ions and aqueous species is the dielectric constant. The dielectric constant of water is the parameter that provides a measure of how well a solvent is able to dissolve an ionic substance. Like the density, the dielectric constant also exhibits a sharp drop at the pseudo-critical point as shown in Figure 1(c). As well, this drop is reduced and becomes smoother as system pressure is increased. This drastic change in the dielectric constant as the critical point is traversed is extremely important as many solutes that are normally soluble in water become insoluble once the solvent becomes supercritical.

The ionization constant of water is also affected by changing temperature. Figure 1 (d) illustrates the change of the neutral pH of water as temperature is increased. This is of significance because the presently envisaged CANDU-SCWR would likely operate under neutral water conditions. From Figure 1 (d), as with the preceding properties of water, the change in pH is not as pronounced as the system pressure is increased.

### 3. Candidate Materials

Steels and nickel-base alloys are the two broad families of candidate materials that have been identified for use, with possible modifications, in the construction of a SCWR. The family of steels can be broken into two groups: austenitic steels and ferritic-martensitic (F/M) steels. The austenitic steels are a potential choice due to their relatively low weight gain due to corrosion and oxidation. However, they are much more susceptible to stress corrosion cracking (SCC) than the F/M steels. Additionally, oxide spallation is a problem for austenitic steels. This is problematic as particle release into the potentially small tolerances in the SCWR is unacceptable. On the other hand, F/M steels are less susceptible to both SCC and spalling. The F/M steels possess low thermal expansion along with high thermal conductivity. They are also resistant to radiation-induced cracking. However, these steels grow thick oxides and the rate of oxide growth increases with increasing temperature. As a result, these steels have unacceptable corrosion rates and are unsuitable for use with small tolerances [4].

The nickel-base alloys are attractive because of their high temperature strength as well as their minimal oxide growth above the critical point. The drawback for this group is that they are susceptible to cracking in SCW, particularly to irradiation-assisted SCC [4]. As well, if used in-core, the potential for helium embrittlement exists through the transmutation reactions of nickel to iron through neutron capture followed by alpha decay.

### 4. Magnetite and Nickel(II) Oxide Solubilities

A previous study by the authors theoretically predicted the solubilities for magnetite,  $\text{Fe}_3\text{O}_4$ , and nickel(II) oxide,  $\text{NiO}$ , over a range of temperatures for several pressures [5]. For each system, several dissolved ions and aqueous species were selected. For the magnetite-water system, the following species were considered:  $\text{Fe}^{2+}$ ,  $\text{FeOH}^+$ ,  $\text{Fe}(\text{OH})_2^+$ ,  $\text{Fe}(\text{OH})_3^-$ ,  $\text{Fe}(\text{OH})_4^-$ ,  $\text{Fe}(\text{OH})_{2(\text{aq})}$  and  $\text{Fe}(\text{OH})_{3(\text{aq})}$ . Likewise, for nickel(II) oxide,  $\text{Ni}^{2+}$ ,  $\text{NiOH}^+$ ,  $\text{Ni}(\text{OH})_3^-$  were the ionic species used along

with  $\text{Ni}(\text{OH})_{2(\text{aq})}$  as the neutral species present in a dissolved solution. Thermodynamic data for all of the species under consideration was obtained from Beverskog and Puigdomenech [6,7]. Estimation of the solubility of these oxides requires a calculation of the Gibbs Free Energy of reaction for the various dissolution equilibria established at the required temperature and pressure. To facilitate this calculation, the semi-empirical revised Helgeson-Kirkham-Flowers (R-HKF) model was employed through a MATLAB computer code built in-house. This results in a series of interdependent equations for each system that are compiled and solved using the overall charge balance in solution (for calculation details, see reference 5).

Using this model, the solubilities for magnetite and nickel oxide under neutral pH conditions were computed over typical temperature ranges for four different operational pressures. These are illustrated in Figure 3(a) and 3(b) respectively:

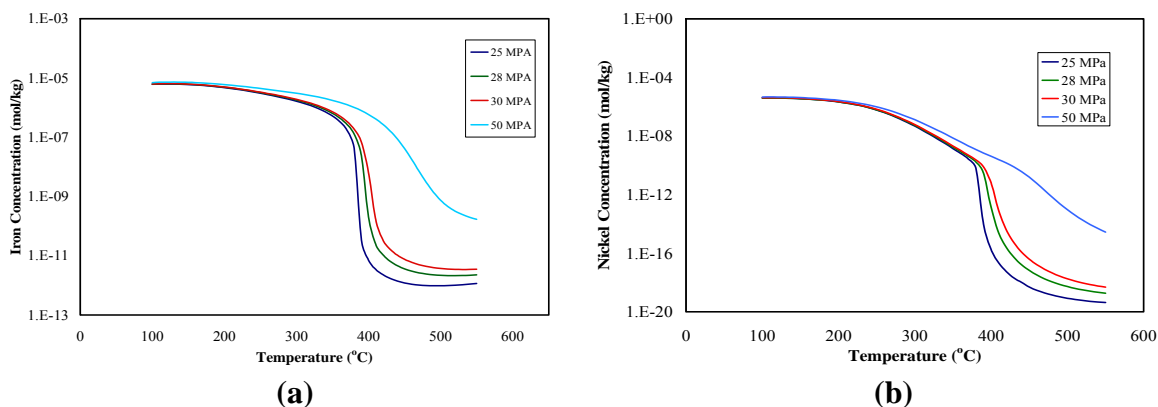


**Figure 3. Predicted solubility of (a) magnetite and (b) nickel(II) oxide as a function of temperature and pressure.**

From Figure 3(a) and (b), several trends are observed. First, the solubilities for both oxides decrease dramatically as the critical point is traversed. As pressure is increased, there is little effect on solubility under subcritical conditions but the solubility increases with increasing pressure above the critical point. Finally, it should be noted that nickel oxide exhibits much lower solubilities in SCW for a given pressure as compared to magnetite and can be considered effectively insoluble. The calculated values for total dissolved iron using this model are approximately an order of magnitude higher at 300°C and 10 MPa than those reported by Tremaine and LeBlanc [8] but are within the range for the Sweeton and Baes dataset [9]. For further discussion, see reference 5.

## 5. Transport Model

The model used in this study is an extension of the corrosion-product transport and deposition model developed for PWR conditions by Cook [9] and for SCWR conditions by Fatoux [10]. In the present study, the fuel cladding and liner are assumed to be made of Inconel 625. The model assumes that chromium is immobile in the alloy and remains within the inner oxide layer; however this may be an invalid assumption under SCWR conditions, particularly in-core, due to the presence of oxidising species from the radiolytic decomposition of water. For simplicity, the volume of metal corroded is assumed to be replaced by a chromite layer,  $\text{NiCr}_2\text{O}_4$ , consuming all the chromium available while nickel oxide,  $\text{NiO}$ , is assumed to replace the remaining volume corroded. The corroded material that does not form this inner layer diffuses to the oxide-solution interface where it either deposits as the outer oxide layer or is carried into the bulk solution. This process is dependent upon the mass transport

properties and the saturation level of the bulk coolant and the water in the boundary layer established between the metal and the solution. Mass transport properties are estimated through heat transfer correlations for supercritical water conditions and applying the Chilton-Colburn analogy between heat and mass transfer to determine the Sherwood number and mass transfer coefficient. Saturation levels are calculated as the solubility of the oxides as described above.

Three mechanisms govern the balance of corrosion products at the oxide-solution interface: dissolution/deposition from/to the surface oxides, mass transfer to the bulk solution, and diffusion through the inner oxide layer due to corrosion. Assuming Inconel 625 is the material of construction, the amount of nickel contained in the inner oxide layer ( $InNi_{inconel}$ ) is estimated as:

$$InNi_{inconel} = 0.445 \frac{dm_{Ni}}{dt} (1 - \theta) \quad (1)$$

where  $dm_{Ni}/dt$  is the total corrosion rate of nickel from Inconel 625,  $\theta$  is the inner oxide porosity (assumed in this study to be 0.01), and 0.445 is fraction of nickel in the inner oxide film multiplied by the ratio of oxide density to alloy density.

The thickness of the inner oxide layer is found from the mass fraction of nickel contained in the inner layer:

$$\frac{d\delta_i}{dt} = 0.793 \frac{dm_{Ni}}{dt} (1 - \theta) \quad (2)$$

The iron and fraction of nickel that does not form the inner oxide layer diffuse to the oxide-solution surface, which is represented by equations 3 and 4:

$$OutFe = 0.086 \frac{dm_{Ni}}{dt} \quad (3)$$

$$OutNi = 0.445 \frac{dm_{Ni}}{dt} (1.25 + \theta) \quad (4)$$

The deposition or dissolution of iron/nickel is computed using a first order kinetic expression where the driving force is the difference between the ion concentration in the interface and the ion concentration at saturation (i.e. solubility):

$$\frac{d\delta_o}{dt} = K_d (C_{o/s} - C_{sat}) \quad (5)$$

$K_d$  is the deposition or dissolution constant and  $C_{o/s}$  is the concentration of iron or nickel ( $kg/m^3$ ) in the metal/solution interface given by equation 6 where  $h$  is the mass transfer coefficient (m/s). If the concentration of iron or nickel in the oxide-solution interface is lower than the solubility, the oxide dissolves and hence,  $K_d$  is the dissolution constant (m/s). Conversely,  $K_d$  is the deposition constant when the solubility is lower than the concentration in the oxide-surface interface. Unfortunately, experimental values for these kinetic constants are limited under conditions of the current generation of reactors and are unknown under supercritical conditions. For lack of further information, this study has assumed  $K_d$  to be 0.001 m/s for both the dissolution and deposition cases and is considered a variable parameter in the model. This is taken to be higher than the dissolution constant measurements of magnetite from Balakrishnan under conventional CANDU operating conditions due to the significant increase in temperature for the SCWR system [12].

$$C_{o/s} = \frac{outNi(orFe) + K_d C_{sat} + hC_{bulk}}{K_d + h} \quad (6)$$

For this model, the 5.7 m long fuel channel is divided into 57 equal increments. Entering bulk concentrations for both iron and nickel are inputted into the first segment and concentrations for subsequent segments are calculated through equation 7:

$$C_{bulk}(x+1) = C_{bulk}(x) + \frac{4h}{Ud_{flow}}(C_{o/s}(x) - C_{bulk}(x)) \times length \quad (7)$$

where U is the coolant velocity (m/s) in the increment of interest, and  $d_{flow}$  is the equivalent diameter of the fuel channel (m). The SCWR fuel channel parameters used in the model were chosen to match those in reference 13.

A corrosion rate of 0.1  $\mu\text{m}/\text{year}$  was used in this study for all temperatures since Inconel 625 typically exhibits low corrosion rates under SCW conditions. It should be noted that in actual operation the corrosion rate will not be constant throughout the core due to temperature changes, irradiation effects, and changing coolant properties from subcritical to supercritical conditions; however, as a first approximation, this simplistic corrosion rate has been assumed. Future work will focus on corrosion model development.

## 6. Results of Transport Model

This study examined the effect of the saturation level of the coolant in dissolved iron and nickel on the amount and location of corrosion product deposition in a fuel channel at two different pressures (25 and 50 MPa). It had been previously predicted that coolant saturation level would have a large impact on the magnitude of deposition in the channel [2]. Therefore, the case of saturated coolant continually entering the fuel channel was examined and compared to the situation where the coolant is undersaturated upon entering ( $10^{-8} \text{ kg/m}^3$  for iron and  $10^{-9} \text{ kg/m}^3$  for nickel). This comparison was done for a pressure close to where the CANDU-SCWR will operate (25 MPa) and a much higher pressure (50 MPa) in order to examine the differences caused by increasing pressure in deposition magnitude and onset location.

### 6.1 Saturated coolant entering fuel channel

Figure 4 shows the hypothetical temperature and density profile for the SCW coolant along the fuel channel [14 & 15]:

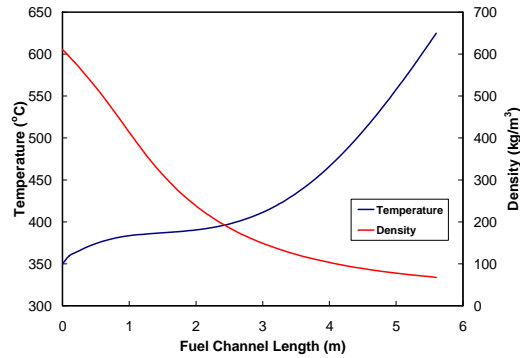


**Figure 4. SCW temperature and density along a CANDU-SCWR fuel channel at 25 MPa.**

The coolant enters the fuel channel at 350°C and the temperature remains below the critical point for approximately the first 1/3<sup>rd</sup> of the channel. The density decreases slowly in this area as the critical point is approached and traversed.

If the coolant is assumed to be saturated in dissolved iron and nickel when entering the fuel channel, then  $C_{\text{bulk}} = C_{\text{sat}}$ . The bulk, oxide-solution interface and saturation concentrations for both metals are plotted in Figures 5 (a) and (b) with position in the fuel channel.

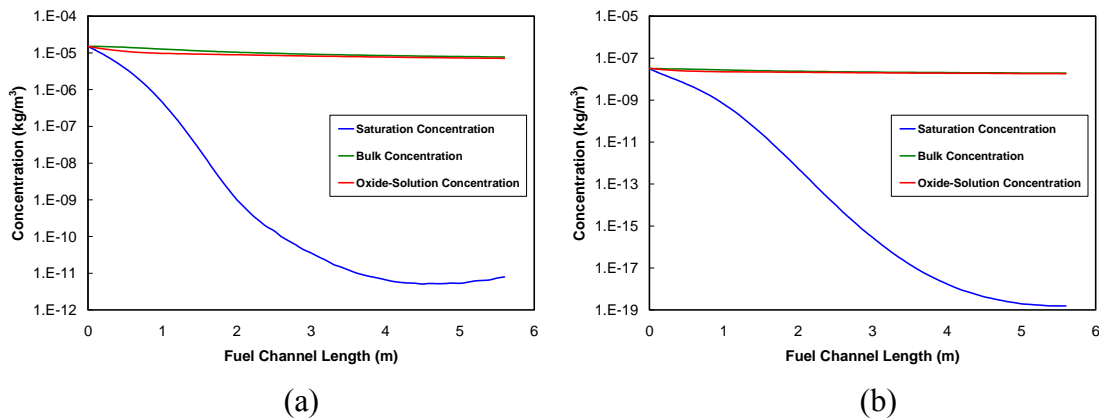


**Figure 5. Saturation and bulk (oxide-solution) concentrations of iron (a) and nickel (b) for saturated coolant entering the reactor core at 25 MPa.**

In saturated conditions, the oxide-solution concentration is effectively equal to the bulk concentration for both iron and nickel. In Figure 5, the bulk and interface concentrations are higher than the saturation concentration throughout the length of the fuel channel. This is expected as the coolant enters saturated while the solubility falls off rapidly for both species as observed in Figure 3.

For one year of operation, the model predicts the deposit loading shown in Figure 6 for a saturated coolant entering the core at 25 MPa and a  $K_d$  of  $10^{-3}$  m/s:

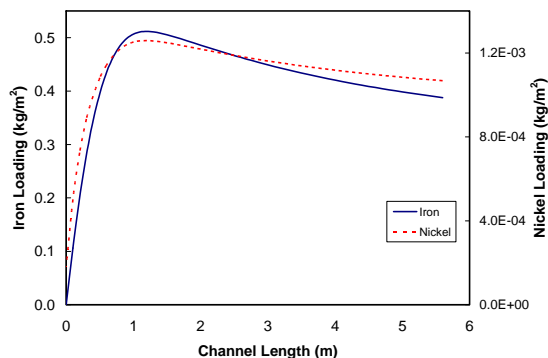


**Figure 6. Loading of iron and nickel after 1 yr of operation at 25 MPa.**

After the first metre, the deposition of iron and nickel reaches a maximum and gradually decreases along the fuel channel, with the loading of nickel being approximately three orders of magnitude lower than for iron. The lower amount of nickel can be explained by the fact that the bulk concentration of nickel is roughly three orders of magnitude lower than that of iron. Because the oxide-solution concentration is effectively equal to the bulk concentration and is much greater than the saturation concentration, oxide precipitation is the predominant process and the surfaces in the reactor core would be coated with an oxide deposit, approximately 100  $\mu\text{m}$  thick, over the first year of operation.

## 6.2 Undersaturated coolant entering the fuel channel

To examine the effect of water undersaturated in dissolved iron and nickel entering the fuel channel, the initial concentrations of iron and nickel in the first increment were set to  $10^{-8} \text{ kg/m}^3$  and  $10^{-9} \text{ kg/m}^3$  respectively, values corresponding to the use of low corrosion materials in the feed train or the use of appropriate water chemistry, as is done in current power plants. Figure 7 (a) and (b) illustrate the effect of undersaturated coolant on the bulk concentrations of iron and nickel along the fuel channel:

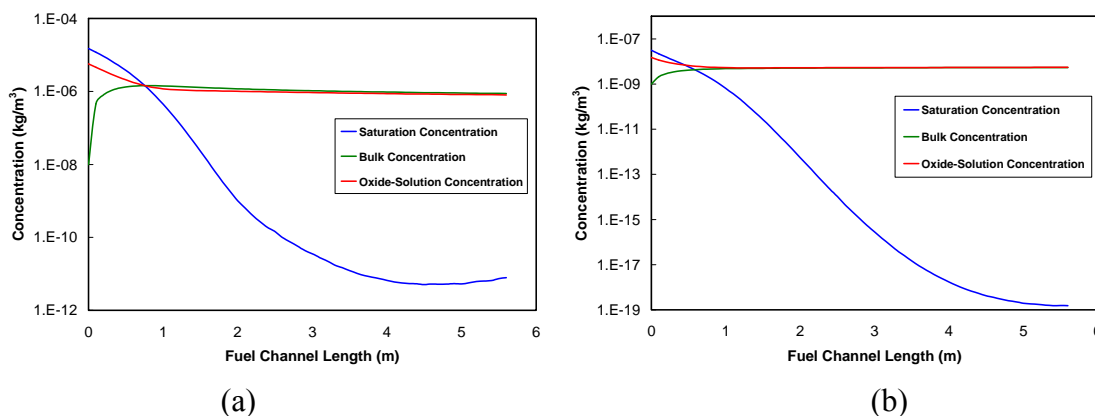


**Figure 7. Saturation, bulk, and oxide-solution concentrations of iron (a) and nickel (b) for undersaturated coolant entering the core at 25 MPa.**

Figure 7 (a) shows that the saturation concentration of iron is higher than both the bulk and oxide-solution concentrations for approximately the first metre of the fuel channel. For nickel, in Figure 7 (b),

the saturation concentration is higher than the oxide-solution concentration until just before the first metre. The loading of precipitated iron and nickel for undersaturated coolant is shown in Figure 8:

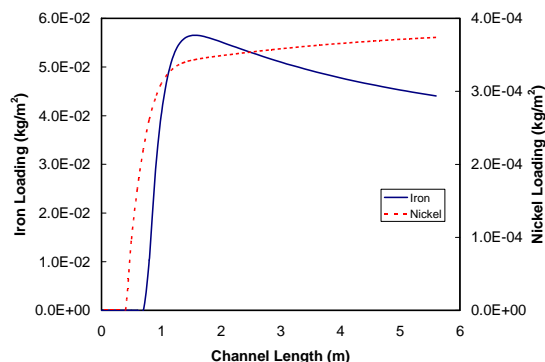


**Figure 8. Loading of iron and nickel in undersaturated coolant after 1 yr of operation at 25 MPa.**

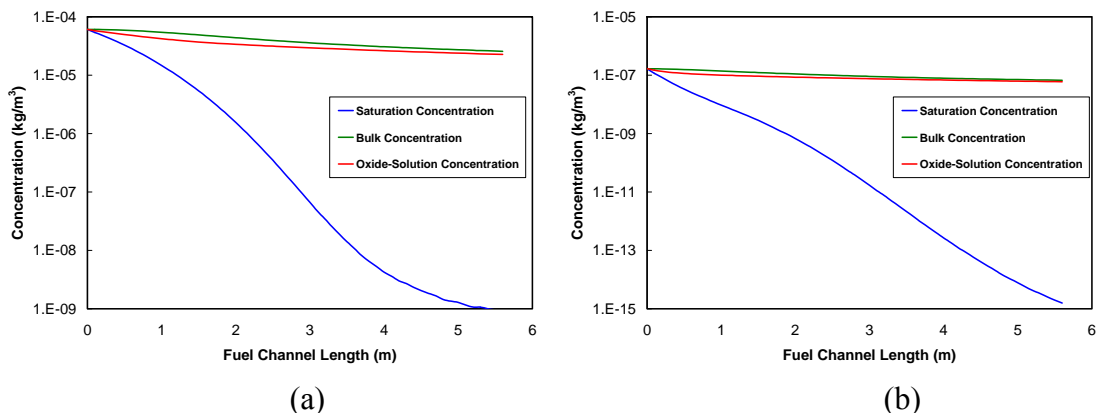
Iron does not begin to deposit until roughly one metre into the fuel channel as shown in Figure 8. This corresponds to point where the oxide-solution concentration becomes greater than the bulk concentration in Figure 7 (a). Because the outer oxide layer dissolves when the interface concentration is lower than the saturation concentration, no deposition would be expected in this region. However, once the saturation concentration falls below the value at the oxide-solution interface, precipitation will occur as shown by the plots in Figure 8. It should also be noted that the magnitude of iron loading is approximately 2 orders of magnitude less at its maximum than that found under the saturated conditions described in Section 6.1. The maximum loading is reached just before two metres along the channel and then gradually decreases. This is due to the decrease in oxide-solution concentration observed in Figure 7. As the interface concentration decreases, deposition will likewise decrease. For nickel, Figure 8 shows the same basic trend as iron with the onset of deposition at around 0.5 m and an order of magnitude lower loading than that observed under saturated conditions.

### 6.3 Increasing system pressure

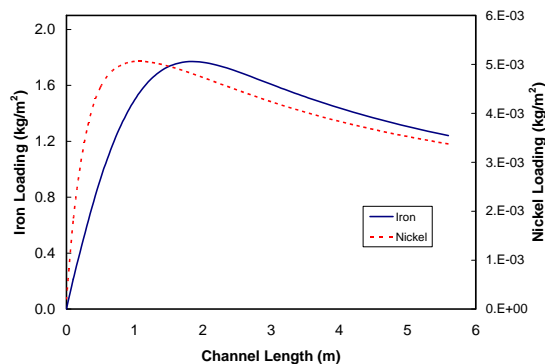
The effect of increasing the operating pressure of the SCWR was also considered. From Figure 3, when the operating pressure is raised to 50 MPa, the solubilities of iron and nickel are both predicted to increase and exhibit more gradual declines as the critical point is traversed. Figure 9 illustrates the predicted effect of operating at 50 MPa for the bulk and saturation concentrations along the channel for iron and nickel with the coolant entering saturated.

For both iron and nickel, the oxide-solution concentration is slightly lower than the bulk concentration. Due to the increase in solubility from the increase in pressure, all the concentrations are higher for iron and nickel in Figures 9 (a) and (b) along the length of the fuel channel when compared to Figures 5 (a) and (b) at 25 MPa. The deposit loading at 50 MPa is shown in Figure 10.

In Figure 10, the deposition trends for iron and nickel are similar to those observed in Figure 6. However, the amount of deposition on the fuel is significantly higher for 50 MPa as shown in Figure 10. This is because the increase in pressure increases both the saturation concentration and likewise the bulk concentration (since the coolant enters saturated). These relative increases compared to the 25 MPa case should correspond to a relative increase in maximum loading of iron from  $\sim 0.5 \text{ kg/m}^2$  to  $\sim 1.8 \text{ kg/m}^2$  as illustrated in Figure 10.



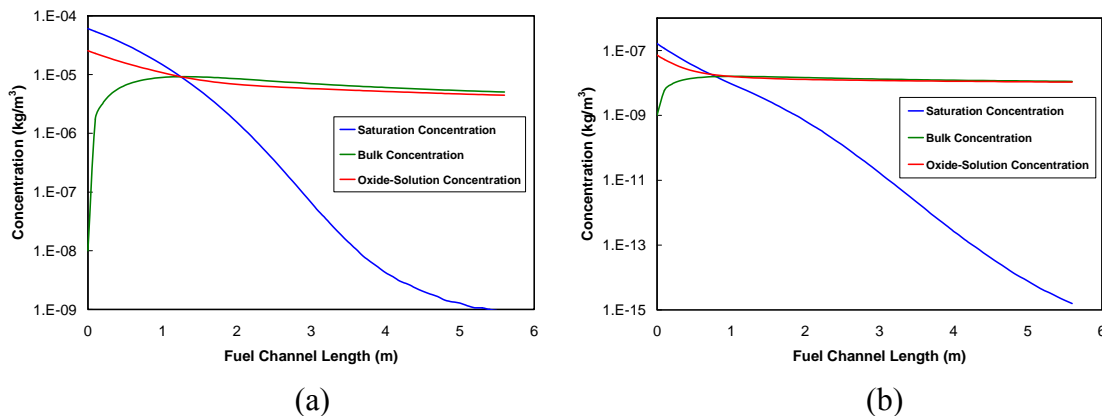
**Figure 9. Saturation and bulk concentrations of iron (a) and nickel (b) for saturated coolant entering the core at 50 MPa.**



**Figure 10. Deposit loading of iron and nickel along a fuel channel with saturated coolant after one year of operation at 50 MPa.**

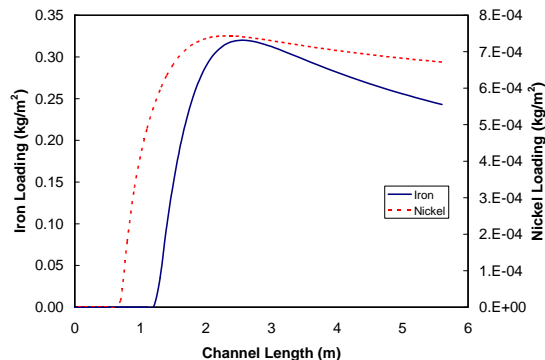
#### 6.4 Higher pressure with undersaturated coolant

The behaviour of saturation, bulk, and oxide-solution concentrations of iron and nickel at 50 MPa with an undersaturated coolant ( $10^{-8}$  kg/m<sup>3</sup> for iron and  $10^{-9}$  kg/m<sup>3</sup> nickel) entering the channel is illustrated in Figure 11:



**Figure 11. Saturation, bulk, and oxide-solution concentrations of iron (a) and nickel (b) for undersaturated coolant entering the core at 50 MPa.**

Figure 11 (a) shows the oxide-solution concentration for iron equals the saturation concentration at approximately one quarter of the fuel channel length (1.5 m). This represents a shift from Figure 7 (a) where the transition occurred at roughly 1/6<sup>th</sup> of the length (1 m). Nickel, on the other hand, exhibits in Figure 11 (b) basically the same trend observed in Figure 7 (b) with the interface concentration exceeding the bulk slightly before the first metre. The deposition trends are depicted in Figure 12.



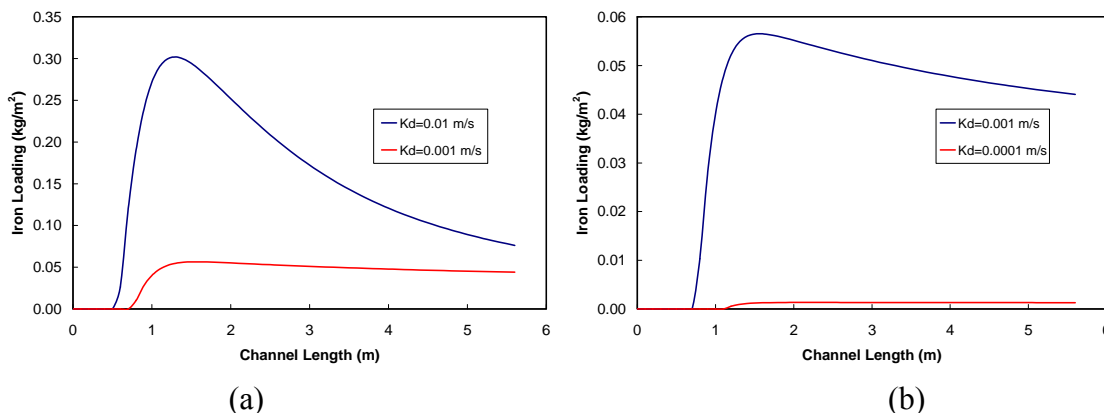
**Figure 12. Deposit loading of iron and nickel along a fuel channel with undersaturated coolant after 1 year of operation at 50 MPa.**

Figure 12 shows a drop off in deposition after a distance of 2.0 m for nickel with the onset of deposition occurring further along the channel compared to Figure 8. This is expected as the oxide-solution concentration exhibited more of a decline for nickel as the pressure was increased and did not become greater than the bulk concentration until just before the first metre. The iron loading experienced two noticeable changes. First, the amount of loading is about an order of magnitude higher for 50 MPa. Secondly, there is a shift in the initiation of iron deposition to a location approximately one quarter way through the channel. These results are consistent with expectations from Figure 10 (a) where the concentrations are higher due to the increase in pressure but, like nickel, the intersection between saturation and interface concentrations does not occur until roughly one quarter along the channel.

### 6.5 Changing Precipitation Rate Constant ( $K_d$ )

This study assumed a value of 0.001 m/s for the deposition and dissolution constants. However, this is a guess as the deposition kinetics are unknown for supercritical conditions. Figure 13 illustrates the effect on iron loading for both an order of magnitude increase and decrease of  $K_d$  in undersaturated coolant ( $10^{-8}$  kg/m<sup>3</sup>) at 25 MPa.

Increasing  $K_d$  to 0.01 m/s increases the maximum loading by a factor of six with the highest deposition occurring along the second metre of the channel as shown in Figure 13 (a). The decrease in loading after the maximum is much steeper for the higher kinetic constant. Figure 13 (b) shows a much larger difference (~40 times) in maximum deposition as  $K_d$  is decreased to 0.0001 m/s. The trends displayed in Figure 13 show the importance knowing the kinetic constants for magnetite deposition in supercritical water. An order of magnitude shift in either direction can have a dramatic effect on deposition in the fuel channel. This highlights the need for additional research to determine the kinetic constants for corrosion product deposition and dissolution in supercritical water. Such work is being planned at UNB.



**Figure 13. Effect of (a) increasing and (b) decreasing  $K_d$  by an order of magnitude on iron deposit for undersaturated coolant at 25 MPa.**

## 6.6 Potential Operation Strategies

It is apparent from this preliminary study that coolant saturated in dissolved iron and nickel entering a SCWR fuel channel is unfavourable for plant operation. The loading of precipitated iron was three orders of magnitude lower for undersaturated coolant. As a result, mitigation of the release of dissolved corrosion-products in the feed train should be a primary focus of SCWR development and design. As suggested by Guzonas et al. [15, 16], this could involve use of more corrosion resistant alloys instead of the commonly used carbon steels for much of the feedwater system in order to minimize the corrosion product release into the coolant. Also, optimizing the water chemistry is common practice and effectively reduces the solubility and hence corrosion rate of materials of construction. However, care must be taking if selecting a pH control additive since they will most likely be ineffective above the critical point and may present further issues in the downstream locations of a SCWR.

It was observed that increasing operational pressure had an undesirable effect in terms of crud loading. The deposition trends along the fuel channel remained the same as in the lower pressure case but the magnitude of deposition was significantly higher. Therefore, in terms of crud deposits, the lower pressure should be used. On the other hand, operating at a higher pressure, while not affecting nickel deposition in this study, did shift the location at which the initiation of deposition of iron occurred. Hence, while some parts of the channel would experience increased total loading, the total surface area where deposition occurs would be reduced with an increasing operational pressure.

## 7. Conclusions

A corrosion-product transport model was developed using the proposed SCWR operating conditions along with solubilities of iron and nickel at the temperatures and pressures of interest estimated using the revised Helgeson-Kirkham-Flowers model and a uniform I625 corrosion rate of 0.1  $\mu\text{m}/\text{year}$ . The corrosion product model demonstrated that dissolved concentrations of iron and nickel in the coolant play a large role in determining loading along the fuel channel. For iron, saturated coolant produced a loading that gradually decreased throughout the length of the fuel channel whereas undersaturated coolant delayed the initiation of deposition until approximately 1/6<sup>th</sup> of the distance in the channel for 25 MPa. Increasing the operational pressure of the SCWR to 50 MPa resulted in higher levels of iron deposits but shifted the initiation of deposition further along the channel. This study reveals the need to control dissolved iron and nickel species entering the reactor core from corrosion and corrosion release

from the feedwater train, in addition to the need for further R&D to determine kinetics of corrosion product deposition/dissolution in high-temperature and supercritical conditions.

## 8. Acknowledgements

The authors thank the NSERC/NRCan/AECL Generation IV Technologies Program for the funding to carry out this work and Dave Guzonas and Matt Edwards for helpful discussions.

## 9. References

- [1] D.F. Torgerson et al, "CANDU Technology for Generation III+ and IV Reactors", *Nucl. Eng. Design*, Vol. 236, 2006, pp.1565-1572.
- [2] K.A. Burrill, "Water Chemistries and Corrosion Product Transport in Supercritical Water in Reactor Heat Transport Systems, 8<sup>th</sup> International Conference of Water Chemistry of Nuclear Reactor Systems, Bournemouth, United Kingdom, 2000.
- [3] L. Qiu and D. Guzonas, "An Overview of Corrosion Product Solubilities in Subcritical and Supercritical Water", 2<sup>nd</sup> Canada-China Joint Workshop on Supercritical Water-Cooled Reactors, Toronto, Ontario, Canada. 2010.
- [4] G. S. Was et al., "Corrosion and Stress Corrosion Cracking in Supercritical Water", *Journal of Nuclear Materials*, Vol. 371, 2007, pp.176-201.
- [5] W.G. Cook and R.P. Olive, "Potential Chemistry and Operational Strategies to Minimize Corrosion-Product and Activity Transport in a CANDU®-SCWR", NPC-2010, Quebec City, Quebec, Canada, 2010.
- [6] B. Beverskog and I. Puigdomenech, "Revised Pourbaix Diagrams for Iron at 25-300°C", *Corrosion Science*, Vol. 38, 1996, pp.2121-2135.
- [7] B. Beverskog and I. Puigdomenech, "Revised Pourbaix Diagrams for Nickel at 25-300°C", *Corrosion Science*, Vol. 39, 1997, pp.969-980.
- [8] P.R. Tremaine and J.C. LeBlanc, "The Solubility of Magnetite and the Hydrolysis and Oxidation of Fe<sup>2+</sup> in Water to 300°C", *J. Solution Chemistry*, Vol.9, 1980, pp.415-442.
- [9] F.H. Sweeton and C.F. Baes, "The Solubility of Magnetite and Hydrolysis of Ferrous Ion in Aqueous Solutions at Elevated Temperatures", *J. Chemical Thermodynamics*, vol.2, pp.479-500, 1970.
- [10] W.G. Cook, "Experiments and Model of General Corrosion and Flow-Assisted Corrosion of Materials in Nuclear Reactor Environments", UNB PhD Thesis, 2005.
- [11] W. Fatoux, "A CANDU-SCWR with a Steam Generator: Preliminary Thermodynamic Assessment and Estimation of Fouling Rates", UNB Masters Thesis, 2009.
- [12] P.V. Balakrishnan, "A Radio Chemical Technique for the Study of the Dissolution of Corrosion-Products in High Temperature Water", *Canadian J. Chem. Eng.*, Vol. 55, 1977, pp.357-360.
- [13] M. Nadin, S. Mokry, and I. Pioro, "SCW NPPs: Layouts and Thermodynamic Cycles", *Nuclear Energy for New Europe*, Bled, Slovenia, 2009.

- [14] M. Edwards, Private communication, AECL, June 2010.
- [15] D. Guzonas and M. Edwards, “Strategies for Corrosion Monitoring and Control in a CANDU©-SCWR”, *2<sup>nd</sup> Canada-China Joint Workshop on Supercritical Water-Cooled Reactors*, Toronto, April 2010.
- [16] D. Guzonas et al., “Corrosion of Candidate Materials for Use in a Supercritical Water CANDU® Reactor”, *13<sup>th</sup> International Conference on Environmental Degradation of Materials in Nuclear Power Systems*, Whistler, British Columbia, 2007.